EARTHQUAKE ENGINEERING AND STRUCTURAL DYNAMICS
Earthquake Engng Struct. Dyn. 2006; **35**:1167–1185
Published online 16 May 2006 in Wiley InterScience (www.interscience.wiley.com). DOI: 10.1002/eqe.579

Evaluating performance of post-tensioned steel connections with strands and reduced flange plates

Chung-Che Chou[1,*,†,‡], Jun-Hen Chen[1,§], Yu-Chih Chen[1,§] and Keh-Chyuan Tsai[2,¶]

[1]*Department of Civil Engineering, National Chiao Tung University, 1001 Ta-hsueh Rd., Hsinchu 300, Taiwan*
[2]*National Center for Research on Earthquake Engineering, Taipei, Taiwan*

SUMMARY

The seismic performance of post-tensioned steel connections for moment-resisting frames was examined experimentally and analytically. Cyclic tests were conducted on three full-scale subassemblies, which had two steel beams post-tensioned to a concrete-filled tube (CFT) column with high-strength strands to provide recentring response. Reduced flange plates (RFPs) welded to the column and bolted to the beam flange were used to increase the dissipation of energy. Test results indicated that (1) the proposed buckling-restrained RFP could dissipate energy in axial tension and compression, (2) the subassemblies could reach an interstorey drift of 4% without strength degradation, and (3) buckling of the beam occurred towards an interstorey drift of 5%, causing a loss of the strand force, the recentring response, and the moment capacity. A general-purpose non-linear finite element analysis program (ABAQUS) was used to perform a correlation study. The behaviour of the steel beam under both post-tensioning and flexural loadings was compared to the test results and predictions. Copyright © 2006 John Wiley & Sons, Ltd.

KEY WORDS: post-tensioned steel connections; strands; reduced flange plates; cyclic tests; finite element analysis

INTRODUCTION

Earlier studies [1–3] showed that the unbonded post-tensioned, precast concrete beam-to-column connection subassemblies can undergo large deformation with a small residual drift.

*Correspondence to: Chung-Che Chou, Department of Civil Engineering, National Chiao Tung University, 1001 Ta-hsueh Rd., Hsinchu 300, Taiwan.
†E-mail: chchou@mail.nctu.edu.tw
‡Assistant Professor.
§Graduate Student Researcher.
¶Director, National Center for Research on Earthquake Engineering and Professor, National Taiwan University.

Contract/grant sponsor: NCREE

Received 15 February 2005
Revised 14 February 2006
Accepted 14 February 2006

Unlike cast-in-place reinforced concrete monolithic connections, the flexural behaviour of such subassemblies was characterized by the opening and closing of the gap at the beam–column interface under cyclic loading. This response could be maintained with the dissipation of only a little energy as long as the strands did not yield and the beam or column was not severely damaged.

Ricles *et al.* [4, 5], Garlock *et al.* [6], and Christopoulos *et al.* [7] applied the same technology to the steel beam-to-column connections. The systems in these studies used high-strength steel strands or bars to provide precompression between the beam and column, and provided seat angles or round bars to increase the dissipation of energy. Different limit states such as angle fracture, strand yielding, and beam local buckling were discussed.

This paper investigates further the cyclic responses of post-tensioned connections with a different energy-dissipating device, the limit state of beam local buckling, and the stress flow in the beam using the finite element computer program (ABAQUS). The beam-to-column subassembly incorporates high-strength bundled strands along with reduced flange plates (RFPs) for energy dissipation. The plate, shop welded to the tube and field bolted outside the beam flange, is able to develop stable energy in both tension and compression when out-of-plane displacement of the RFP is limited. Experimental investigation shows that the proposed connection is able to achieve similar hysteretic behaviour comparable to the post-tensioned connection with either seat angles or round bars. Beam local buckling, however, occurs at a strain level less than reported by Garlock *et al.* [6]. The finite element analysis demonstrates that the longitudinal stresses in the beam subjected to both post-tensioning and bending actions be predicted if the effect of stress concentration in the beam in initial post-tensioning is included.

OBJECTIVE

This work attempts to achieve the following: (1) investigate experimentally the behaviour of three post-tensioned connections with two steel beams and a concrete-filled tube (CFT) column; (2) examine how much the energy dissipation can be increased with the reduced flange plate (RFP) provided in the connection, and (3) perform a correlation study with a general-purpose non-linear finite element analysis program (ABAQUS) to compare local stresses to the test results and predictions.

DESIGN OF TEST SPECIMEN

Figure 1(a) shows a frame, which incorporates high-strength steel strands that are anchored outside the exterior CFT column and RFPs that are used to increase energy dissipation of the connection. The experimental program [8] involved tests of three full-scale subassemblies, each of which was composed of a CFT column ($350 \times 350 \times 9$) and two steel beams ($W450 \times 200 \times 9 \times 14$). ASTM Grade 345 (50 ksi) steel was specified for the beam and column tube; the specified 28 day concrete strength was 35 MPa. The width-thickness ratio of the beam flange was 7.1 less than the limiting width-thickness ratio λ_{ps} ($= 0.30\sqrt{E_s/F_y} = 7.2$), based on the AISC Seismic Provisions [9]. The width-thickness ratio of the web was 45,

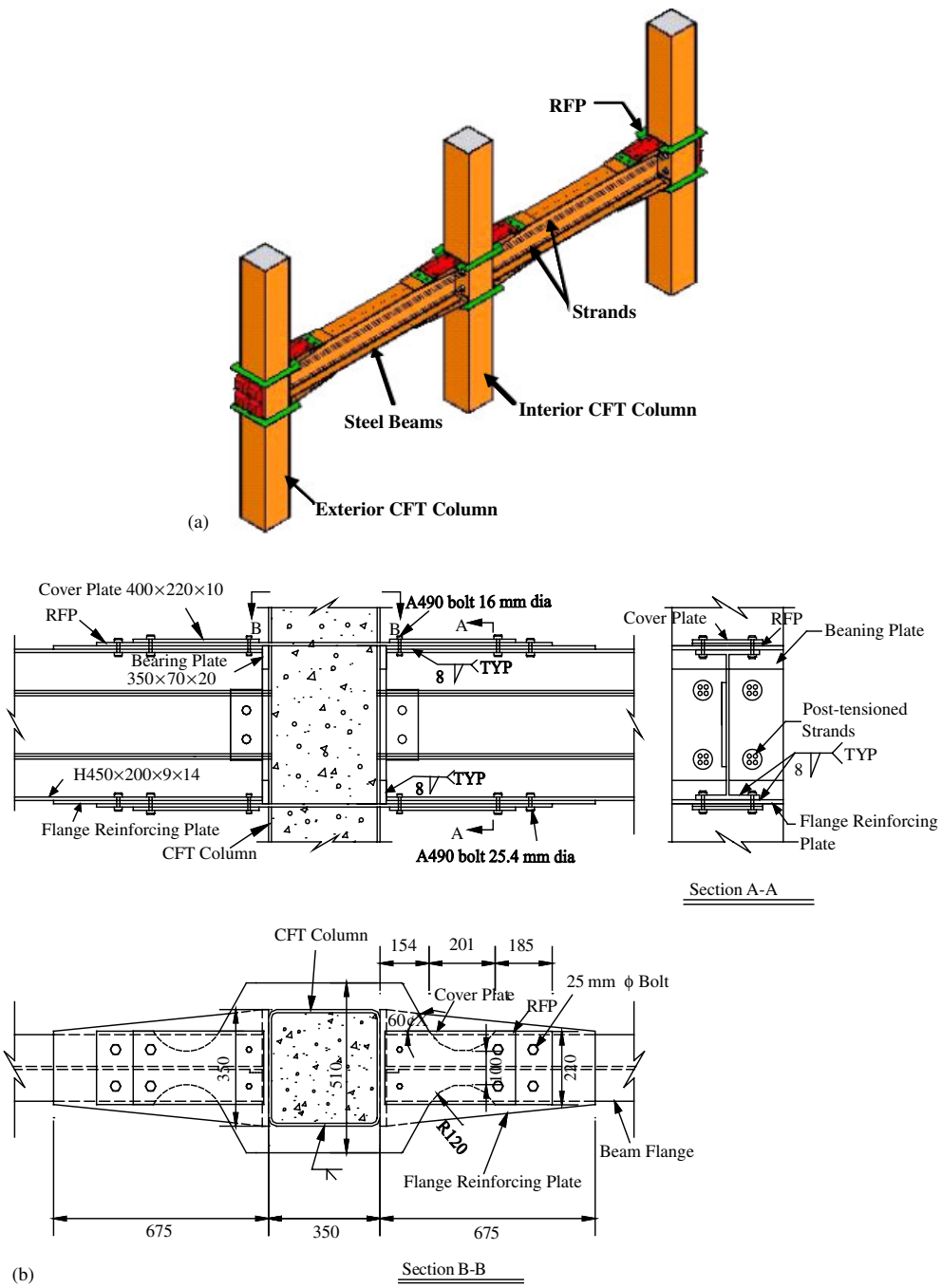

Figure 1. Proposed post-tensioned beam-to-CFT column connection: (a) frame with post-tensioned strands and RFPs; and (b) specimen 3 connection details.

Table I. Test matrix.

Specimen no.	T_0 (kN)	$\frac{T_0}{T_{ST,u}}$	t_R (mm)	Cover PL. (mm)	$\frac{M_d}{M_{np}}$	$\varepsilon_{R,0.02}$	$\frac{M_{0.02}}{M_{np}}$	$\frac{P_{0.04}}{\phi_b P_y}$	Beam buckling θ_g (rad)
1	968	0.33	—	No.	0.31	—	0.51	0.65	—
2	968	0.33	5	No.	0.38	0.08	0.72	0.65	0.039
3	968	0.33	8	10	0.42	0.08	0.80	0.65	0.035

Note: $T_{ST,u}$ = ultimate strand force, M_{np} = nominal plastic moment of the beam, P_y = yield strength of the beam, $\phi_b = 0.9$.

indicating that the maximum axial load demand–capacity ratio ($P_u/\phi_b P_y$) of the web in combined flexure and axial compression should not exceed 0.66, which was determined as

$$\frac{P_u}{\phi_b P_y} \leqslant 2.33 - \frac{h/t_w}{1.12\sqrt{E_s/F_y}} = 0.66 \tag{1}$$

where h, t_w, E_s, and F_y are the depth of the beam web, the thickness of the beam web, the modulus of elasticity of the steel and the yield strength of the steel, respectively. This ratio was used to limit the maximum compression force in the steel beam. Figure 1(b) shows details of an interior beam-to-CFT column connection. Four DYWIDAG multistrand tendons, two of which are placed on each side of the web and pass through the column, provide the post-tensioning force. A tendon contains four 13 mm diameter seven wire, uncoated, low-relaxation ASTM A416 Grade 270 strands. The modulus of elasticity and tensile strength provided by the manufacturer are 195 GPa and 1860 MPa, respectively.

These specimens were designed to investigate the energy dissipation of the connection with the RFPs and the limit state of beam local buckling. Table I summarizes the test matrix. All specimens had 16 strands and total initial post-tensioning force, T_0 (968 kN). Specimen 1 was designed when only high-strength strands were present; Specimens 2 and 3 also had the RFPs bolted outside the flange reinforcing plates. The thicknesses, t_R, of the RFPs of Specimens 2 and 3 were selected to be 5 and 8 mm, respectively, but a cover plate (10 mm thick) was bolted outside the RFP of only Specimen 3 to prevent the RFP from buckling under compression. Therefore, the effect of out-of-plane restraining on energy dissipation of the RFPs could be examined. The RFP shape shown in Figure 1(b) and steel grade (A36) remained the same in both specimens; the narrowest section was designed based on expected moment contribution (αM_{np}) and a tensile strain, $\varepsilon_{R,0.02}$, of 0.08 at a target gap opening angle, θ_g, of 0.02 rad. The notation of M_{np} is defined as the nominal plastic moment of the beam. Slot holes were made in the RFP near the column to allow horizontal movement of 16 mm-diameter bolts.

The experimental investigation [4, 7] described clearly the need for flange reinforcing plates and bearing plates, so that all specimens had them in the study. The flange reinforcing plates, 5 mm thick for Specimen 1 and 12 mm thick for Specimens 2 and 3, were tapered and fillet welded outside the beam flange (Figure 1(b)). The length (675 mm) of the flange reinforcing plate was the same for all specimens so that yielding in Specimens 2 and 3 beam flanges at the end of the flange reinforcing plates was expected to occur about the target gap opening angle. The bearing plates were $350 \times 70 \times 20$ mm, fillet welded to the end of the flange reinforcing plate, beam flange, and beam web.

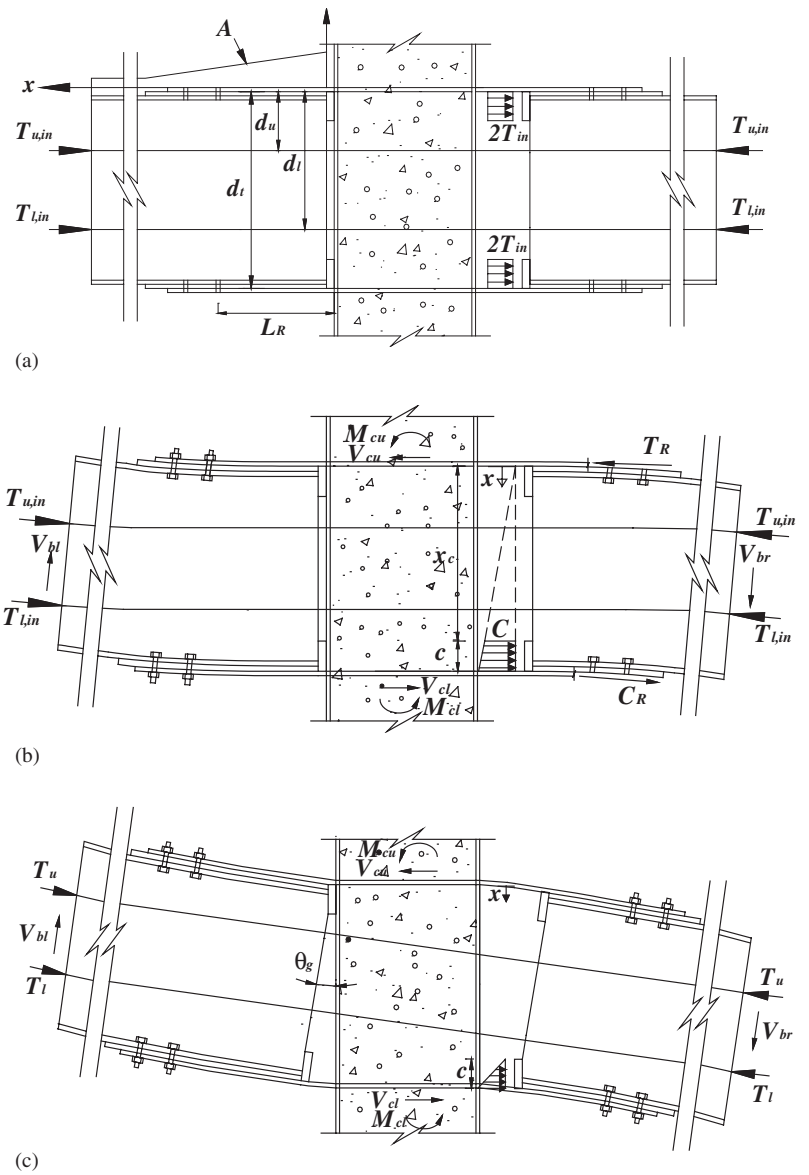

Figure 2. Behaviour of post-tensioned beam-to-column connection: (a) initial post-tensioning stage; (b) forces contributing decompression moment; and (c) gap opening.

Decompression moment

Figure 2(a) shows the free-body of the connection under initial post-tensioning force. One of the beams is placed away from the face of the column to show the stress distribution in the bearing plate. The shortening of the beam flange section, which is a distance L_R from the

face of the column, is estimated as

$$\Delta_{\text{in}} = \int_0^{L_R} \frac{4T_{\text{in}}}{E_s \times A}\,\mathrm{d}x \tag{2}$$

where A is the cross-sectional area of the beam plus flange reinforcing plates, the areas of which vary along the beam length (Figure 1(b)). The post-tensioning forces, $T_{\text{u,in}}$ and $T_{\text{l,in}}$, in the upper and lower strands are assumed to be T_{in}. Note that the RFPs are stress-free before applying beam shear because they are bolted to the beam flange after the application of the post-tensioning force.

Figure 2(b) shows the deformation of the connection just before the gap between the beam–column interface opens; the compression force, C, and the decompression moment, M_{d}, are

$$C = \int_{x_c}^{d_t} E_s \left(2\varepsilon_f \frac{x}{d_t}\right) \mathrm{d}A = 2T_{\text{u,in}} + 2T_{\text{l,in}} = 4T_{\text{in}} \tag{3}$$

$$\begin{aligned} M_{\text{d}} &= M_{\text{ST}} + M_{\text{ERFP}} \\ &= \left[\int_{x_c}^{d_t} E_s \left(2\varepsilon_f \frac{x}{d_t}\right) x\,\mathrm{d}A - 2T_{\text{u,in}} d_{\text{u}} - 2T_{\text{l,in}} d_{\text{l}}\right] + \left[C_R\left(d_t + \frac{t_R}{2}\right) + T_R \frac{t_R}{2}\right] \\ &= \left[\int_{x_c}^{d_t} E_s \left(2\varepsilon_f \frac{x^2}{d_t}\right) \mathrm{d}A - 2T_{\text{in}} d_t\right] + [C_R(d_t + t_R)] \end{aligned} \tag{4}$$

where M_{ST} and M_{ERFP} are the moments provided by the strands and the RFPs, respectively; t_R is the thickness of the RFP; d_t $(= d_{\text{u}} + d_{\text{l}})$ is the sum of the beam depth and the thickness of the flange reinforcing plates; d_{u} is the distance between the upper strand and the top flange reinforcing plate, and d_{l} is the distance between the lower strand and the top flange reinforcing plate. The strain, ε_f, was estimated from the total initial post-tensioning force, bearing area at the end of the beam, and the modulus of elasticity of the steel. Prior to decompression, the post-tensioning forces, $T_{\text{u,in}}$ and $T_{\text{l,in}}$, in the strands do not change noticeably from the initial value, T_{in}; the tension force, T_R, and the compression force, C_R, in the RFPs are assumed to be the same and determined based on the axial deformation, Δ_{in}, in Equation (2). To obtain the relationship between the axial force and deformation of the RFP, the axial stress–strain relationship of the steel is approximated by a bi-linear relationship, as shown in Figure 3(a). The yield force, $P_{R\text{y}}$, and the ultimate force, $P_{R\text{u}}$, are determined as the smallest sectional area of the RFP (Figure 3(b)) times the yield strength, σ_{y}, and times the ultimate strength σ_{u}, respectively. The corresponding axial yield deformation, Δ_{y}, and the ultimate deformation, Δ_{u}, are calculated by integrating the strain over the length L_R from the column face. For simplicity, the axial force–deformation relationship of the RFP is also approximated by a bi-linear relationship, as shown in Figure 3(c).

Moment-gap opening angle relationship following decompression

Considering strand elongation and beam shortening following decompression (Figure 2(c)), the strand forces, T_{u} and T_{l}, in the upper and lower strands are assumed to be T_{ST}, and are

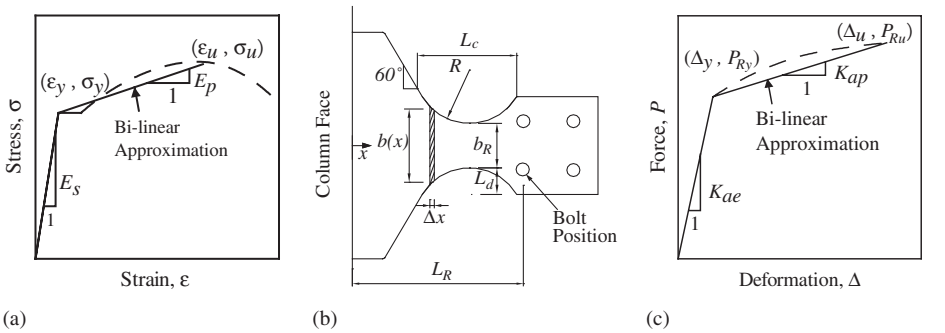

Figure 3. RFP axial force–deformation relationship: (a) σ–ε relationship; (b) RFP cut-out; and (c) P–Δ relationship.

given by

$$T_{ST} = T_{in} + \Delta T = T_{in} + \left[\frac{2(d_t/2 - c)\theta_g}{L_{ST}}\left(1 - \frac{4A_{ST}}{A_b + 4A_{ST}}\right)\right] E_{ST}A_{ST} \tag{5}$$

where A_b is the cross-sectional area of the beam; c is the position of the neutral axis at the beam end; A_{ST} is the cross-sectional area of four 13 mm diameter strands; E_{ST} is the modulus of elasticity of the strand; θ_g is the gap opening angle between the beam–column interface, and L_{ST} is the length of the strands (or the length of one bay).

Assuming a rigid-body rotation of the beam about the neutral axis, the deformations, Δ_t and Δ_c, of the RFPs in tension and compression, respectively, are estimated as

$$\Delta_t = \Delta_{in} + \left(d_t + \frac{t_R}{2} - c\right)\theta_g \tag{6}$$

$$\Delta_c = \Delta_{in} + \left(\frac{t_R}{2} + c\right)\theta_g \tag{7}$$

where Δ_{in} and the second term in the equations are used to estimate the deformation of the RFP before and after decompression, respectively. Figure 3(c) is then used to determine the axial forces of the RFPs based on the deformations in Equations (6) and (7).

The position of the neutral axis, c, and the moment corresponding to a given gap opening angle, θ_g, are determined from an iterative beam sectional analysis:

1. Assume a position of the neutral axis, c, at the end of the beam.
2. Compute the strand force using Equation (5) and the axial forces in the RFPs using Equations (6), (7), and Figure 3(c).
3. Construct a linear normal strain profile with the maximum compression strain ε_{max} at the flange reinforcing plate of the beam and zero at the neutral axis. The relationship between ε_{max} and the position of the neutral axis c can be found in Christopoulos *et al.* [7]. Compute the resulting normal stresses using the individual stress–strain relationships and integrate the normal stresses over the respective areas to obtain the corresponding forces in the beam.

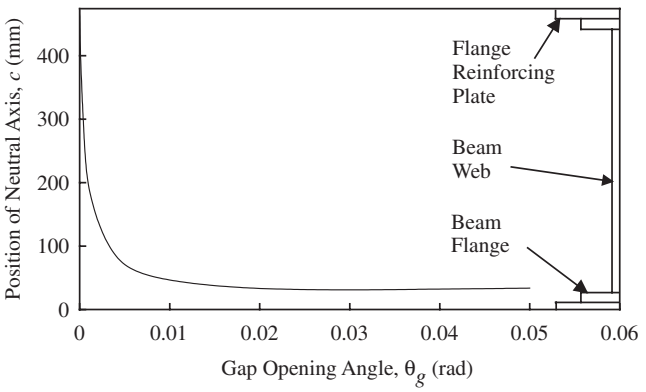

Figure 4. Position of neutral axis versus gap opening angle relationship.

4. Sum the normal forces and check for horizontal force equilibrium.
5. Iterate over a new c by returning to step 1 until horizontal force equilibrium is satisfied. Compute the moment corresponding to the given gap opening angle.

Table I shows the moment, $M_{0.02}$, and post-tensioning force, $P_{0.04}$, calculated at a gap opening angle of 0.02 and 0.04 rad, respectively; the axial load demand–capacity ratios, $P_{0.04}/\phi_b P_y$, are less than 0.66 from Equation (1). The position of the neutral axis, c, obtained from the analysis is a function of the gap opening angle and close to the junction between the beam web and the flange beyond $\theta_g = 0.015$ rad (Figure 4).

Flexural stiffness of the post-tensioned beam with RFPs

Because the position of the neutral axis approaches to the junction between the beam web and flange, this position is used to evaluate the stiffness of the post-tensioned beam after decompression. Figure 5 shows the relationship between the beam moment and the inter-storey drift, θ, which is computed by dividing the beam tip deflection by the length, L, to the centreline of the CFT column. The precompression provided by the strands ensures full contact between the beam and the column before decompression. The moment–interstorey drift relationship exhibits elastic behaviour, which has the initial flexural stiffness similar to that in a fully restrained moment connection [5]. Hence, the elastic flexural stiffness of the post-tensioned beam, K_b, is approximated using that of a fully restrained beam [10]

$$K_b = \frac{3E_s I_b L}{L_b^2} \tag{8}$$

where I_b is the moment of inertia of the beam and L_b is the beam length measured from the column face. The elastic flexural stiffness provided by the RFPs, K_{ERFP}, is computed as

$$K_{ERFP} = K_b \frac{M_{ERFP}}{M_{ST}} = K_b \frac{C_R(d_t + t_R)}{\int_{x_c}^{d_t} E_s \left(2\varepsilon_f \frac{x^2}{d_t}\right) dA - 2T_{in} d_t} \tag{9}$$

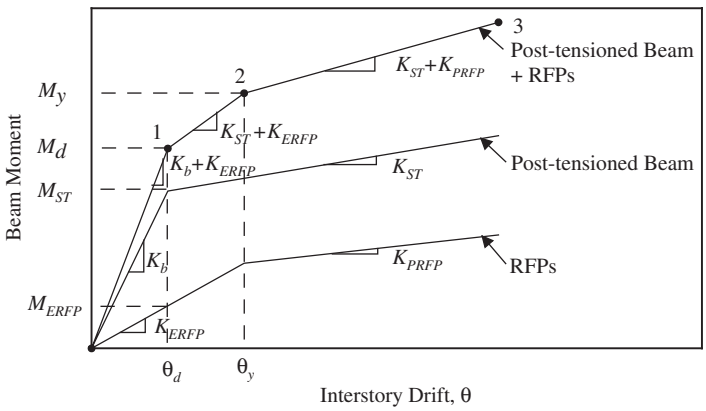

Figure 5. Flexural stiffness of post-tensioned beam with RFPs.

Prior to decompression, the flexural stiffness of the post-tensioned beam with elastic RFPs equals the sum of the stiffness K_{b} and K_{ERFP}.

Decompression begins at Step 1 after which the flexural stiffness of the post-tensioned beam is contributed by the post-tensioning strands and the beam. If the beam is assumed to rotate about the junction between the beam flange and the web, the increment in moment provided by the strands is

$$\Delta M = 4\Delta T d_c = 4\left[E_{\mathrm{ST}}A_{\mathrm{ST}}\frac{2d_c\Delta\theta_{\mathrm{g}}}{L_{\mathrm{ST}}}\left(1-\frac{4A_{\mathrm{ST}}}{A_{\mathrm{b}}+4A_{\mathrm{ST}}}\right)\right]d_c = K_{\mathrm{ST},t}\Delta\theta_{\mathrm{g}} \tag{10}$$

where d_c is the distance between the beam centreline and the junction and $K_{\mathrm{ST},t}$ is the flexural stiffness provided by the strands. The flexural stiffness of the post-tensioned beam, K_{ST}, following decompression can be estimated as

$$K_{\mathrm{ST}} = \frac{1}{\dfrac{1}{K_{\mathrm{b}}}+\dfrac{1}{K_{\mathrm{ST},t}}} \tag{11}$$

As loading is increased, the RFP yields at Step 2. The inelastic flexural stiffness provided by the RFPs is

$$K_{\mathrm{PRFP},t} = \frac{\Delta M}{\Delta\theta_{\mathrm{g}}} = (d_1^2+d_2^2)K_{ap} \tag{12}$$

where d_1 is the distance from the top RFP to the junction; d_2 is the distance from the bottom RFP to the junction, and K_{ap} is the inelastic axial stiffness of the RFP shown in Figure 3(c). Considering the elastic flexural stiffness of the RFP, K_{PRFP} as shown in Figure 5 can be determined. The flexural stiffness of the post-tensioned beam with inelastic RFPs equals the sum of K_{ST} and K_{PRFP}.

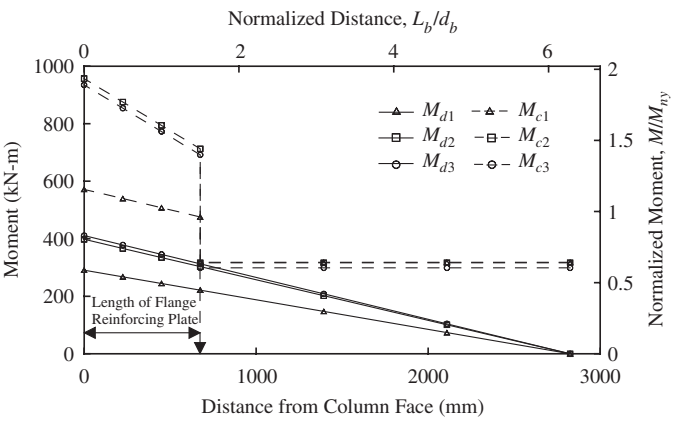

Figure 6. Comparison of moment demands and capacities ($\theta_g = 0.02$ rad).

Flange reinforcing plate

The post-tensioning force is transferred to the column through part of the beam following decompression (Figure 2(c)), so all specimens have flange reinforcing plates to minimize the yielding and potential buckling of the beam flanges. The length of the flange reinforcing plate is determined to limit the beam flange strain at the end of the flange reinforcing plate to the yield strain at the target gap opening angle of 0.02 rad. Figure 6 shows the moment distributions M_{d1}, M_{d2}, and M_{d3} along the length of the beam for Specimens 1, 2, and 3, respectively. The moment capacities M_{ci} ($i = 1, 2$, and 3 for Specimens 1, 2, and 3) are calculated when the beam flange yields under corresponding axial force, T_{ST}

$$M_{ci} = \left(\sigma_y - \frac{T_{ST}}{A}\right)\frac{2I}{d_b} \tag{13}$$

where d_b is the depth of the beam and I is the moment of inertia of the beam plus those of flange reinforcing plates, which vary along the beam length. The intersection of M_{di} and M_{ci} indicates the required minimum length of the flange reinforcing plate. The length (675 mm) of the flange reinforcing plate is used for three specimens. Yielding in Specimens 2 and 3 beam flanges at the end of the flange reinforcing plates is expected to occur at the target gap opening angle. Considering equilibrium of the axial force and bending moment in the beam, Table I lists the gap opening angle when the beam flange near the end of the flange reinforcing plate reaches two times the yield strain, ε_y. The strain value of $2\varepsilon_y$ [6] indicates the onset of beam local buckling.

RFP design criteria and expected connection performance

Since the RFPs increase not only the energy dissipation but also the moment resistance, the RFPs are sized based on the expected moment contribution (αM_{np}) and a tensile strain, $\varepsilon_{R,0.02}$ (0.08), at the target gap opening angle. The value of $\varepsilon_{R,0.02}$ is computed from the elongation of the RFP, the corresponding RFP force (Figure 3(c)), the smallest sectional area

Table II. Behaviours of connections with different RFPs and post-tensioning forces.

Case no.	b_R (mm)	t_R (mm)	T_0 (kN)	$\frac{M_{ST}}{M_{np}}$	$\frac{M_{ERFP}}{M_{np}}$	$\frac{M_d}{M_{np}}$	$\frac{M_{ST}}{M_d}$	$\frac{M_{0.02}}{M_{np}}$	α	$\varepsilon_{R,0.02}$	$\frac{P_{0.04}}{\phi_b P_y}$
1	50	5	968	0.32	0.05	0.37	0.86	0.66	0.07	0.11	0.65
2	100	5	968	0.32	0.06	0.38	0.84	0.72	0.13	0.08	0.65
3	100	8	968	0.32	0.10	0.42	0.76	0.80	0.21	0.08	0.65
4	100	8	1100	0.36	0.11	0.47	0.77	0.85	0.21	0.08	0.69
5	150	8	1100	0.36	0.12	0.48	0.75	0.95	0.31	0.07	0.69

Note: $L_R = 355$ mm, Radius of cut $R = 120$ mm.

(Figure 3(b)), and the stress–strain relationship of the steel (Figure 3(a)). The value of αM_{np} must always be smaller than M_{ST}, generated by the initial post-tensioning forces, to ensure full re-centring of the connection. The steps required to determine the size of the RFP corresponding to the target gap opening angle are:

1. Assume the thickness, t_R, and length, L_R, of the RFP (Figure 3(b)).
2. Estimate the required width, b_R, of the RFP based on the expected moment contribution, αM_{np}, and stress, F_R, in the RFP corresponding to the strain 0.08

$$b_R \geqslant \frac{\alpha M_{np}}{(d_t + t_R) t_R F_R} \tag{14}$$

3. Estimate the radius of the cut R based on the length of the cut, L_c, and the depth of the cut, L_d, using the geometry of a circular arc relationship

$$R = \frac{4L_d^2 + L_c^2}{8L_d} \tag{15}$$

4. Construct the axial force–deformation relationship of the RFP (Figure 3(c)) based on a bi-linear approximation of the steel stress–strain curve.
5. Compute the deformations of the RFPs by Equations (6) and (7), the corresponding forces in the RFPs, the moment contribution of the RFPs, and $\varepsilon_{R,0.02}$ in the smallest sectional area. Iterate over the thickness t_R and the length L_R by returning to step 1 until the strain $\varepsilon_{R,0.02}$ equal to 0.08 and re-centring criteria are satisfied.

Table II lists the expected performance of the post-tensioned connections with different RFP dimensions and total initial post-tensioning forces, T_0. More than 75% ($= M_{ST}/M_d$) of the decompression moment is contributed from the initial post-tensioning force. The beam moment at the target gap opening angle of 0.02 rad, $M_{0.02}$, ranges from 0.66 to $0.95M_{np}$; meanwhile, the moment contribution (αM_{np}) from the RFPs is proportional to the smallest sectional area. The initial post-tensioning force (1100 kN) causes the axial load demand–capacity ratio ($P_{0.04}/\phi_b P_y$) larger than the limiting value (0.66) at a gap opening angle of 0.04 rad.

EXPERIMENTAL PROGRAM

Each specimen was tested in the setup (Figure 7) by displacing actuators at the ends of the beams through a series of displacement cycles. The displacement history consisted of three

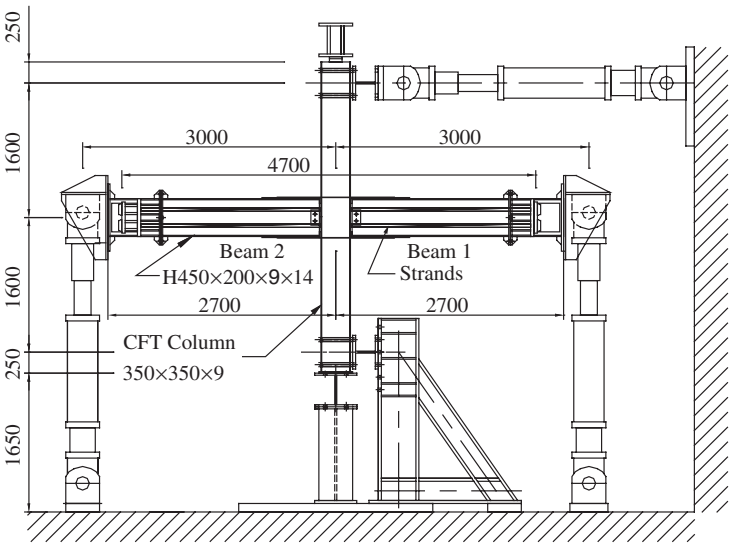

Figure 7. Setup (unit: mm).

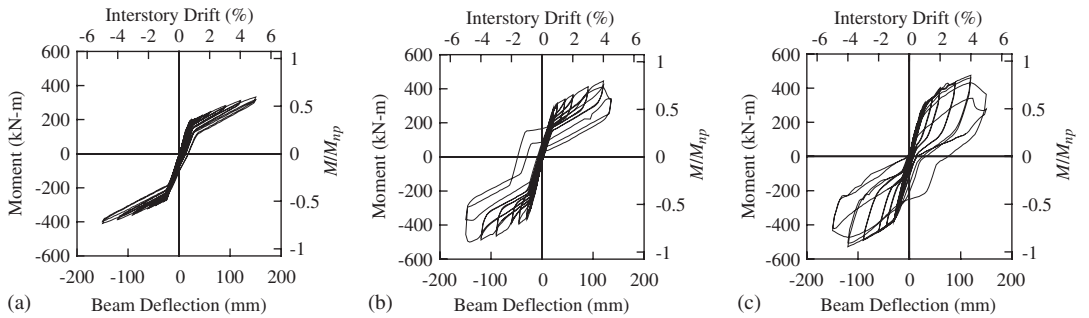

Figure 8. Moment versus beam deflection relationship: (a) Specimen 1; (b) Specimen 2; and (c) Specimen 3.

cycles of interstorey drift with amplitudes of $0.25, 0.375, 0.5, 0.75$ and 1%, followed by two cycles of drift with amplitudes of $1.5, 2, 3, 4$, and 5%.

Figure 8 shows the relationships between the beam tip deflection and the moment for three specimens. The moment and energy dissipation, E_h, of Specimen 3 were higher than that of Specimen 2 (Table III), because buckling of the RFP, which was observed at an interstorey drift of 1% in Specimen 2 test, was delayed to an interstorey drift of 4% in Specimen 3 test by using the cover plate (Figure 9(a)). The area within the hysteresis loops was integrated up to an interstorey drift of 3% to determine E_h, which is the accumulated energy dissipation. The energy dissipation at 4% drift cycles was not included. The ratio of energy dissipation between Specimens 3 and 2 was 3.2 ($=45/14$), larger than the thickness ratio 1.6 ($=8/5$)

Table III. Experimental responses.

Specimen no.	T_0 (kN)	$\frac{T_0}{T_{ST,u}}$	$\frac{M_d}{M_{np}}$	$\frac{M_{0.02}}{M_{np}}$	$\frac{P_u}{\phi_b P_y}$	$\varepsilon_{R,0.02}$	E_h (kN-m)	Beam buckling θ_g (rad)
1	943	0.32	0.31	0.52	0.54	—	9	—
2	982	0.33	0.36	0.71	0.51	0.09	14	0.034
3	943	0.32	0.40	0.74	0.49	0.08	45	0.032

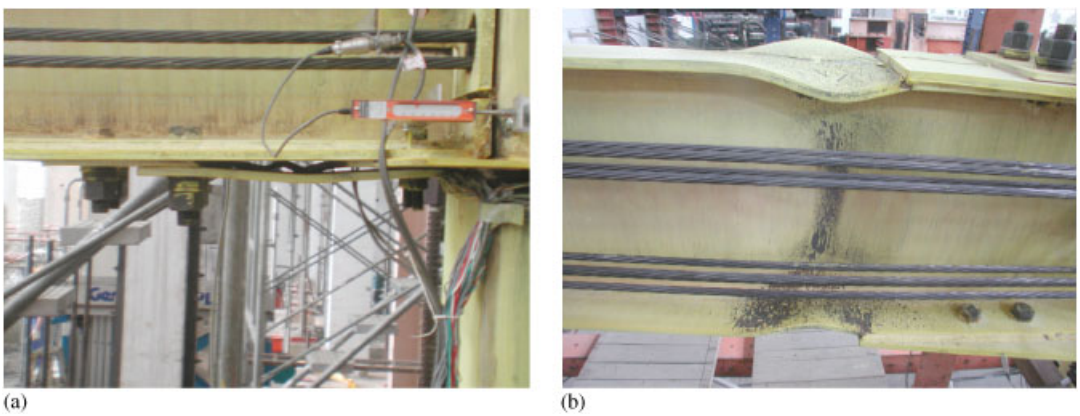

Figure 9. Buckling of RFP and beam (Specimen 3): (a) 4% drift; and (b) 5% drift.

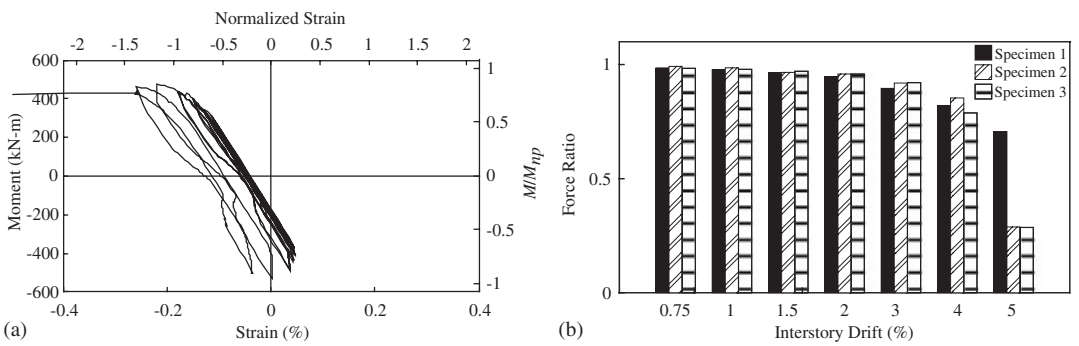

Figure 10. Effect of beam local buckling on subassembly behaviour: (a) moment versus strain relationship (Specimen 3); and (b) strand force ratio versus drift relationship.

of the RFPs. It indicated that the buckling-restrained RFP develops larger energy dissipation than that without out-of-plane restraining. The decompression moment, M_d, the moment at the target gap opening angle, $M_{0.02}$, and the strain, $\varepsilon_{R,0.02}$, in the RFP listed in Table III were close to the predictions listed in Table I.

The gap opening angle, θ_g, was measured with a set of displacement transducers at the beam–column interface. θ_g was 0.023 and 0.022 rad for Specimens 2 and 3, respectively, reaching an interstorey drift of 3%, where yielding was noticed. The beam flange and web in compression buckled locally (Figure 9(b)) at the third time reaching an interstorey drift of 4%, where θ_g was 0.034 and 0.032 rad for Specimens 2 and 3, respectively, smaller than the predictions (Table I). Figure 10(a) shows the relationship between the moment and strain at the beam flange where local flange buckling occurred. It was found that the beam flange developed significant increase in plastic strain after 0.0026 ($=1.4\varepsilon_y$) not $2\varepsilon_y$ reported by Garlock *et al.* [6].

Figure 10(b) shows the ratio of the strand force to the initial post-tensioning force after each drift cycle is completed; the initial post-tensioning force decreases slowly with the yielding of the beam and significantly with the buckling of the beam. The maximum axial load demand–capacity ratios, $P_u/\phi_b P_y$, of Specimens 2 and 3 were about 0.5 (Table III) less than 0.66, based on the AISC Seismic Provisions.

FINITE ELEMENT ANALYSIS

Specimen 1 was modelled with the non-linear finite element analysis program ABAQUS [11] to study the behaviour of the steel beam under combined post-tensioning and flexural loadings. The steel beams and flange reinforcing plates were modelled using four-node shell elements, S4R. Rigid links were incorporated to simulate welding between the beam flange and the flange reinforcing plate. Steel stress–strain relationships obtained from tensile coupon tests were used, and material non-linearity with the von Mises yielding criterion was considered. Since the CFT column remained elastic during the test, the steel tube and concrete infill were modelled as having only elastic properties; eight-node solid elements, C3D8R, were used with full composite action between the steel and concrete. The bearing plate and strands were also modelled using the same eight-node solid elements. Interaction between the bearing plate and the steel tube was modelled with hard and rough contact behaviour, allowing separation of

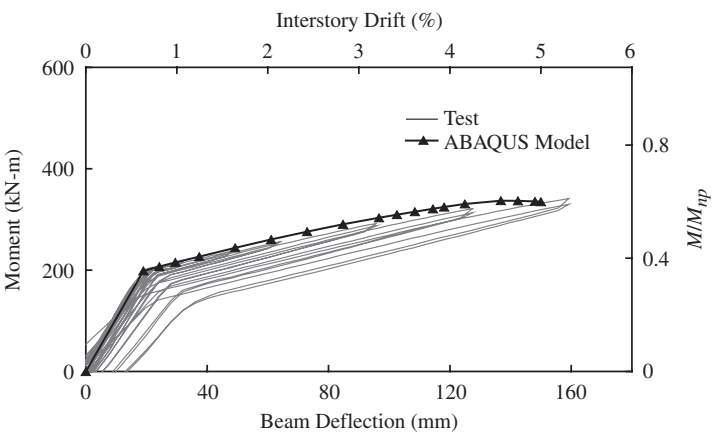

Figure 11. Prediction versus test tesults.

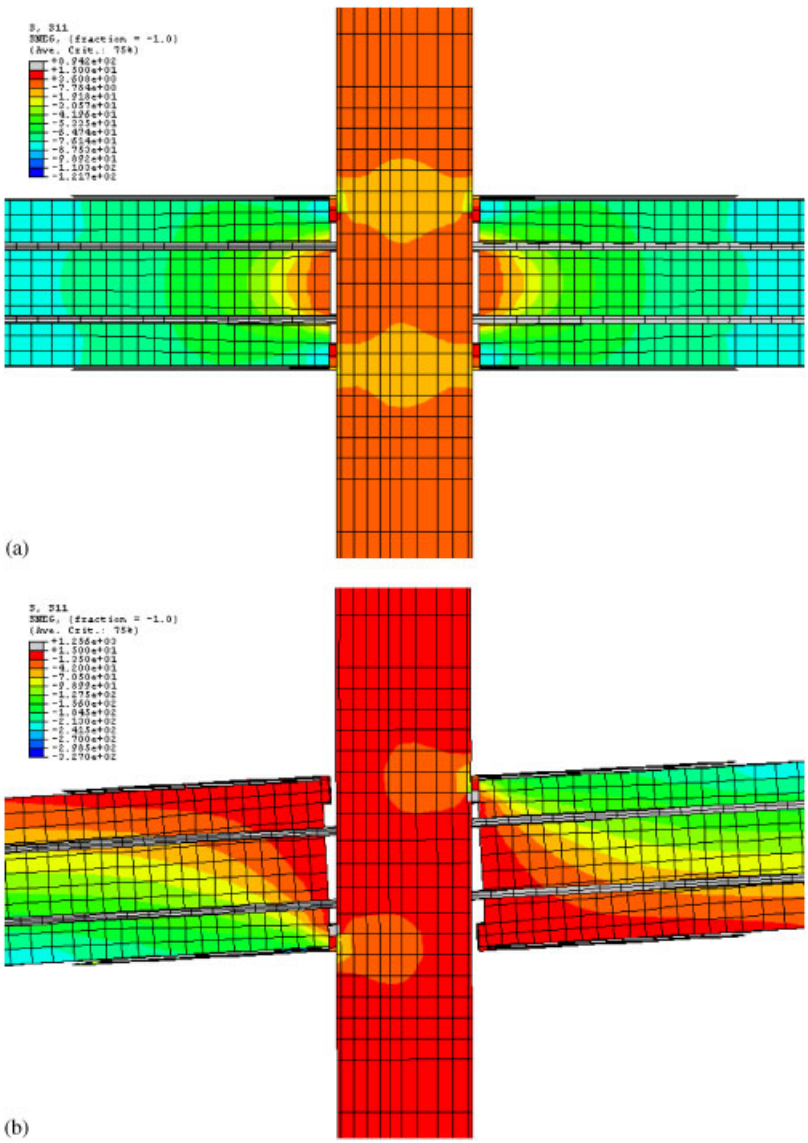

Figure 12. Finite element model (unit: MPa): (a) initial post-tensioning stage; and (b) 2% drift.

the interface in tension and no penetration of that in compression. One end of the strands was connected to the beam end in the step before the application of the beam shear to generate the initial post-tensioning force in the beams and strands.

The predicted beam moment–deflection relationship agrees well with the experimental results, as shown in Figure 11. Figure 12(a) shows the longitudinal stresses in the beam under initial post-tensioning force. The region in which the stress field is disturbed by the bearing

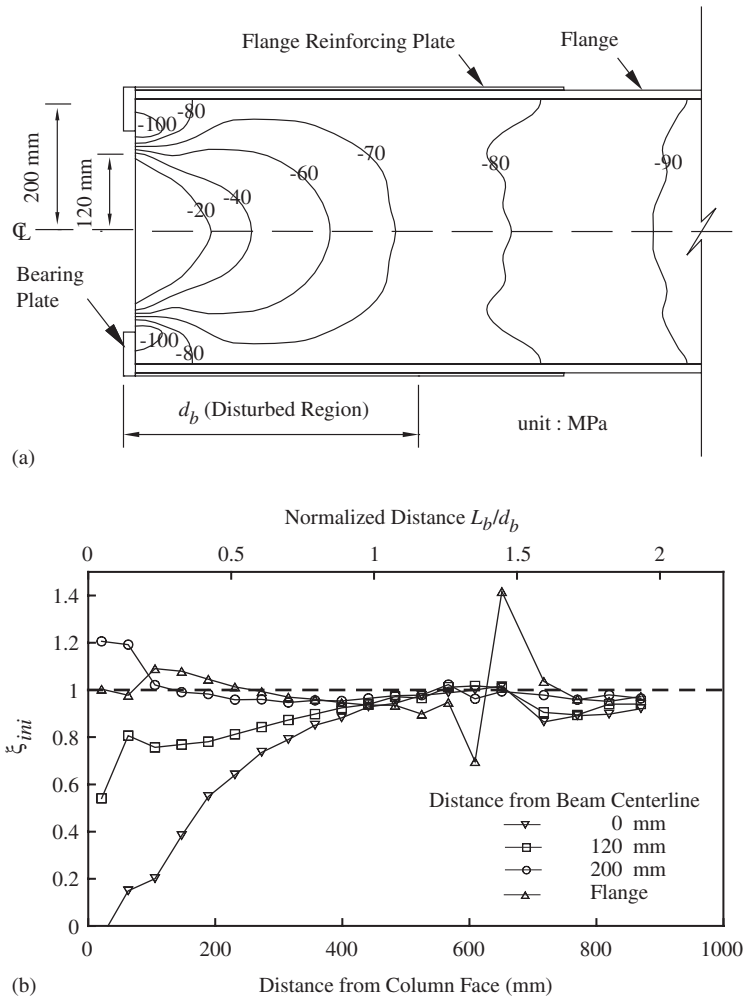

Figure 13. Stress variation in beam under initial post-tensioning force: (a) contour of longitudinal stresses; and (b) stress ratio.

plates extends over a length that is approximately equal, in this case, to the depth of the beam (Figure 13(a)). The flow of stresses in the disturbed region shows that the stresses near the bearing plates are higher and those in the centre part of the beam web are lower. Figure 13(b) shows the ratio, ξ_{ini}, between the stresses determined by the finite element analysis and those computed by dividing the initial post-tensioning force by the cross-sectional area A. The computed stresses were clearly overestimated in the centre part of the beam web and underestimated near the bearing plate.

After the beam–column interface opens, the region on the tension side of the beam has almost zero stress because of the combination of post-tensioning and flexural loadings

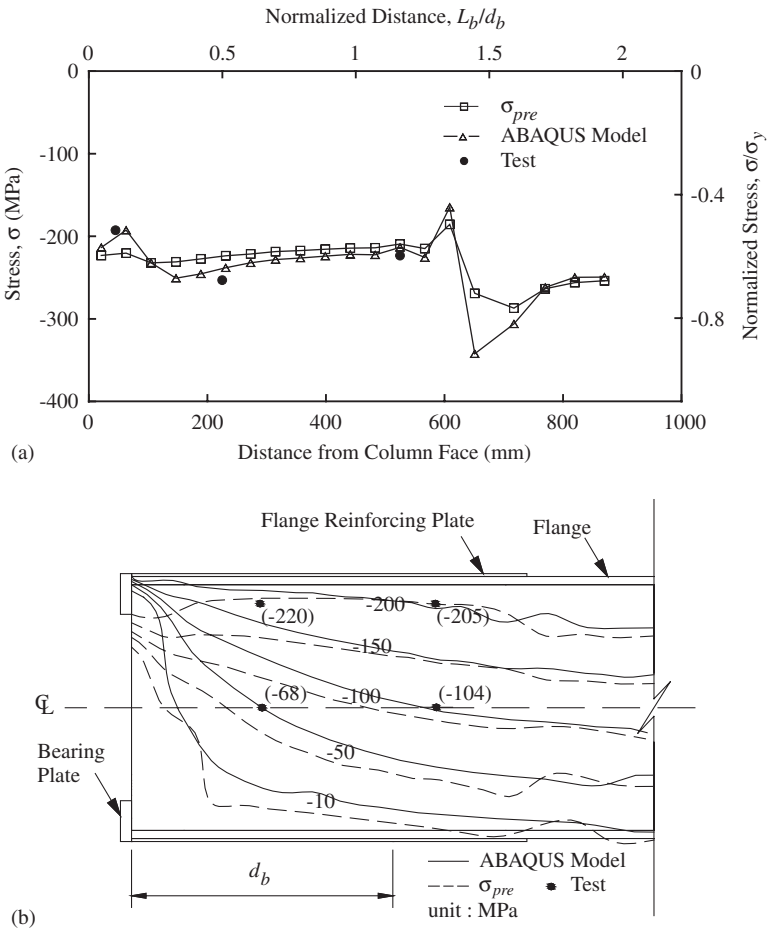

Figure 14. Comparison of longitudinal stress in beam (2% drift): (a) longitudinal stress in beam flange; and (b) contour of longitudinal stress in beam web.

(Figure 12(b)). Figure 14 compares the longitudinal stresses obtained from the model with those determined from the test; the strains caused by the initial post-tensioning force are included in the strain gauge data based on Figure 13. These data are also compared with those predicted by

$$\sigma_{\text{pre}} = \xi_{\text{ini}} \frac{T_{\text{ST}}}{A} + \frac{My}{I} \tag{16}$$

where y is the distance measured from the beam centerline and M is the moment. Figure 14(b) indicates that the longitudinal stresses flow into the junction between the web and the flange and that the stresses can be predicted except the region near the bearing plate.

CONCLUSIONS

Three post-tensioned steel beam-to-CFT column connection subassemblies were tested under cyclic loading to evaluate the seismic behaviour of the connection. Specimen 1 had post-tensioning strands to provide contact between the beams and column. Furthermore, Specimens 2 and 3 incorporated the RFPs (Figure 1) to increase the moment capacity and energy dissipation. The experimental and analytical results support the following conclusions:

(1) Specimens 2 and 3 were designed and verified to remain elastic before the gap opening angle of 0.02 rad, beyond which the steel beam flange yielded at the end of the flange reinforcing plate (Figure 6). The steel beam buckled towards an interstorey drift of 5%, resulting in the loss of the initial post-tensioning force (Figure 10(b)) and the recentring response (Figure 8). The maximum axial load demand–capacity ratios, $P_u/\phi_b P_y$, were about 0.5 (Table III) less than 0.66, based on the AISC seismic provisions. The beam flange strain, near the end of the flange reinforcing plate, was measured to be 1.4 times the yield strain, ε_y, when beam local buckling occurred. This strain value as indicated in Figure 10(a) is slightly less than $2\varepsilon_y$ based on the experiments of Garlock *et al.* [6].
(2) The RFP without out-of-plane restraining yielded in tension and buckled in compression. The buckling-restrained RFP of Specimen 3 was able to yield in tension and compression, dissipating more hysteretic energy than dissipated by Specimen 2 (Table III) before it underwent higher-mode buckling (Figure 9(a)).
(3) Non-linear finite element analysis reasonably predicted the response of Specimen 1 (Figure 11). Before the gap between the beam–column interface opened, the length of the disturbed region associated with the redistribution of stresses was approximately equal to the depth of the beam. The stress ratio, ξ_{ini}, indicated that the centre part of the web was less effective in resisting the compression load (Figure 13). After the gap opened, the longitudinal stresses in the beam except near the bearing plate were predicted by considering ξ_{ini} in the calculation of the axial stresses (Figure 14).

The flag-shaped hysteretic model proposed by Christopoulos *et al.* [12] is representative of the behaviour of the frames incorporating post-tensioned connections both at all beam-to-column connections and at the base of each column. The model with two independent response parameters, α and β, to describe the system response can be used to describe the hysteretic behaviour of the connection if all connections are described with the same parameters and open simultaneously. Parameters, α and β, are 0.13 and 0.61 for Specimen 3. The parameters are the intermediate values of the system in their study, indicating that the system can achieve equal or smaller displacement ductility compared to that of the bilinear elasto-plastic system. Studies of the seismic behaviour of frames with the proposed post-tensioned connections are currently in progress.

ACKNOWLEDGEMENTS

The financial supports provided by the NCREE, Taiwan are greatly appreciated.

REFERENCES

1. Cheok G, Lew H. Model precast concrete beam-to-column connections subject to cyclic loading. *PCI Journal* 1993; **38**(4):80–92.

2. Priestley MJN, MacRae G. Seismic tests of precast beam-to-column joint subassemblages with unbonded tendons. *PCI Journal* 1994; **41**(1):64–81.
3. Pampanin S, Priestley MJN, Sritharan S. Press phase 3: the five-story precast test building-frame direction response. *Report No. SSRP 2000/08*, University of California, San Diego, La Jolla, CA, 2000.
4. Ricles JM, Sause R, Garlock MM, Zhao C. Posttensioned seismic-resistant connections for steel frames. *Journal of Structural Engineering* 2001; **127**(2):113–121.
5. Ricles JM, Sause R, Peng SW, Lu LW. Experimental evaluation of earthquake resistant posttensioned steel connections. *Journal of Structural Engineering* 2002; **128**(7):850–859.
6. Garlock MM, Ricles JM, Sause R. Experimental studies of full-scale posttensioned steel connections. *Journal of Structural Engineering* 2005; **131**(3):438–448.
7. Christopoulos C, Filiatrault A, Uang C-M, Folz B. Posttensioned energy dissipating connections for moment-resisting steel frames. *Journal of Structural Engineering* 2002; **128**(9):1111–1120.
8. Chou C-C, Chen J-H, Chen C-Y. Performance evaluation of post-tensioned steel connections for moment-resisting frames. *6th Korea–Japan–Taiwan Joint Seminar on Earthquake Engineering for Building Structures*, Taiwan, 2004.
9. AISC. *Seismic Provisions for Structural Steel Buildings*. AISC: Chicago, IL, 2002.
10. Englekirk R. *Steel Structures*. Wiley: New York, 1994.
11. HKS. *ABAQUS User's Manual Version 6.3*. Hibbitt, Karlsson & Sorensen, Inc.: Pawtucket, RI, 2003.
12. Christopoulos C, Filiatrault A, Folz B. Seismic response of self-centering hysteretic SDOF systems. *Earthquake Engineering and Structural Dynamics* 2002; **31**(5):1131–1150.

